Hindawi
International Journal of Antennas and Propagation
Volume 2021, Article ID 4580506, 15 pages
https://doi.org/10.1155/2021/4580506

Research Article

Measurements and Characterization for Millimeter-Wave Massive MIMO Channel in High-Speed Railway Station Environment at 28 GHz

Shuangde Li,[1] **Yuanjian Liu**,[1] **Leke Lin**,[2] **and Qi Sun**[1]

[1]*College of Electronic and Optical Engineering, Nanjing University of Posts and Telecommunications, Jiangsu, Nanjing 210023, China*
[2]*National Key Laboratory of Electromagnetic Environment, China Research Institute of Radiowave Propagation, Shandong, Qingdao 266107, China*

Correspondence should be addressed to Shuangde Li; 2016020104@njupt.edu.cn and Yuanjian Liu; liuyj@njupt.edu.cn

Received 19 April 2021; Revised 6 September 2021; Accepted 27 September 2021; Published 26 October 2021

Academic Editor: Mourad Nedil

The millimeter-wave (mmWave) and massive multiple-input multiple-output (MIMO) wireless communication technologies provide vital means to resolve many technical challenges of the fifth-generation (5G) or beyond 5G (B5G) network. Analyzing the measured datasets extracted from the channel measurements can provide insight into the characteristics of radio channels in different scenarios. Therefore, mmWave massive MIMO channel measurements, simulation, and modeling are carried out in the high-speed railway waiting hall environments at 28 GHz. The multipath components (MPCs) parameters are estimated for line-of-sight (LOS) and non-line-of-sight (NLOS) scenarios based on the space-alternating generalized expectation-maximization (SAGE) algorithm. Delay spread (DS), azimuth angle of arrival (AAoA), and elevation angle of arrival (EAoA) are analyzed. And they are processed by using the *K*-mean algorithm. In addition, propagation characteristics are simulated based on the improved ray tracing method of shooting and bouncing ray tracing/image (SBR/IM). The correctness of the improved ray tracing method is verified by comparing the measured results with the simulated results. The large-scale path loss (PL) is characterized based on close-in (CI) free-space reference distance model and the floating-intercept (FI) path loss model. Furthermore, statistical distributions for root-mean-square delay spread (RMS DS) are investigated. The Gaussian distribution best fits the measured data of RMS delay spread. Finally, multipath clustering is identified using the multipath component distance (MCD). The analysis of these results from mmWave massive MIMO channel measurements and simulation may be instructive for the deployment of the 5G or B5G wireless communications systems at 28 GHz.

1. Introduction

The fifth-generation (5G) wireless communication systems will encounter many emerging applications such as ultra-high definition video, connected healthcare, and smart cities [1, 2]. Stimulated by these applications for massive connectivity, 5G wireless communication systems are expected to meet high capacity and high-data-rate transmission demands in different deployment scenarios [3–5]. Millimeter wave (mmWave) frequency bands have large available bandwidths, which can allow the wireless systems to support the enormous increase in capacity demand [6]. Therefore, mmWave communication can be considered one of the potential technologies to meet the requirements for 5G cellular networks [7].

Despite their bandwidth attraction, the free-space path loss (FSPL) increases with the frequency according to the Friis transmission formula. The mmWave channel is strongly influenced by the environmental parameters such as rainfall, foliage, the dimensions of physical obstacles, and scatterers [8, 9]. Massive multiple-input multiple-output (MIMO) can significantly improve the spectrum efficiency [10]. The mmWave frequencies are attracted for massive MIMO due to the very short wavelength [11]. On one hand,

the size of the antenna array can be reduced significantly. On the other hand, the antenna array gains improved by massive MIMO are helpful in overcoming the path loss (PL) of mmWave wireless channel [12–14]. Thus, extensive channel measurements and modeling of the mmWave massive MIMO channel are significant for developing 5G or beyond 5G (B5G) wireless communication systems and performance testing in the hotspot scenarios.

A number of channel models and measurements are investigated for mmWave communications [15–21]. The propagation characteristics of mmWave channel in different outdoor suburban macrocell environments are analyzed at 28 GHz. Combined with antenna pattern, beam misalignment, and obstacle blocking effect, a novel path loss (PL) model is proposed. Small-scale channel parameters such as the number of clusters, delay spread (DS), and angle spread (AS) are extracted [15]. In [16], the broadband directional channel characteristics of millimeter wave transmission in indoor and urban cellular communication systems are measured and analyzed at 28 GHz and 39 GHz. The temporal and spatial channel characteristics are modeled, and a universal channel model is proposed for indoor and urban environments. In [17], the mmWave channel measurements are carried out at 30.4–37.1 GHz, and the second-order statistical characteristics of indoor directional channel are studied. Wideband mmWave indoor propagation measurements are conducted at 28 GHz and 38 GHz for copolarization and cross-polarization antenna configurations [18]. A new radio channel model and channel parameters are derived in terms of various short-range scenarios including offices, a station, and a shopping mall at 60 GHz and 70 GHz [19]. Path loss models and delay spread parameters for different mmWave frequency bands in the corridor environment and in the factory scenario are investigated [20]. In [21], measurements and simulations of mmWave propagation are presented in a rugged underground mine environment.

In addition, mmWave massive MIMO channel measurements and models are studied in [22–29]. In [22], channel measurement campaigns are conducted at 28 GHz, and the space-alternating generalized expectation-maximization (SAGE) algorithm is applied to extract multipath components (MPCs) from the output of a virtual antenna array. Then, the distribution of DS and AS on the virtual vertical plane antenna array is illustrated, and the spatial nonstationary characteristics of massive MIMO antenna array are verified in [23]. The large-scale parameters are researched and multipath parameters are extracted by SAGE based on the outdoor microcell channel measurements at 39 GHz [24]. In addition, it is proved that the channel capacity increases significantly with the increase of the number of antennas by using virtual massive MIMO antenna array [25]. Omnidirectional power delay profile (PDP) is obtained from directional measurements by using the mechanical steering of directive antennas at both transmitter and receiver at 59–65 GHz and 80–86.5 GHz [26]. Moreover, in [27], the vector network analyzer (VNA) and the virtual MIMO antenna array are used to measure the channel in line-of-sight (LOS) and non-line-of-sight (NLOS) scenarios. A statistical propagation channel model is proposed. In [28], the VNA and the uniform rectangular array (URA) are used to carry out measurement of three-dimensional (3D) mmWave MIMO channel in a large conference hall. In [29], DS, AS, eigenvalue, and channel capacity are analyzed based on the acquired massive MIMO channel impulse responses in subway tunnel scenario. However, some hotspot environments are not modeled, e.g., the large stadium or arena, the large waiting hall for airport stations and railway. In [30], an adaptive kernel-power-density (AKPD) algorithm is adopted to identify clusters. The time-evolution characteristics are simulated and validated based on a quasideterministic radio channel generator (QuaDRiGa) simulation platform in a large waiting hall of a high-speed railway station. However, the large-scale path loss models have not been treated by [30] as well as the method of shooting and bouncing ray tracing/image (SBR/IM). To the best of our knowledge, there is a dearth of propagation channel measurements and ray tracing simulations reported in the literature for the high-speed railway waiting hall environment.

With the popularity of high-speed railway at home and abroad, the waiting hall of high-speed railway has become a very representative communication service place for dense crowd. The scenario of high-speed railway waiting hall is the typical indoor scenario of 5G, which has the characteristics of large population density, spacious indoor space, and dense obstacles. Moreover, the wireless channel propagation characteristics in high-speed railway waiting hall environments are different from indoor office and outdoor urban environment. Therefore, extensive measurements and simulations should be conducted in the high-speed railway waiting hall environments at the mmWave frequency band, so as to have a better knowledge of radio propagation characteristics.

The main contributions of this paper are fivefold. First of all, for the large high-speed railway station scenarios, we conduct channel measurements and ray tracing simulations along different routes for LOS and NLOS environments. Second, the propagation characteristics of mmWave massive MIMO channel are investigated at 28 GHz in the large waiting hall at the high-speed railway station. Large-scale path loss and temporal statistics are provided. Third, the path loss models are characterized based on the close-in (CI) free-space reference distance PL model and the floating-intercept (FI) PL model. The comparison between the measured results and simulated results proves that the method of ray tracing simulation is valid. Fourth, the angle dispersion, the received signal energy, and delay spread are analyzed for LOS and NLOS scenarios. Finally, multipath clustering is identified using the multipath component distance (MCD).

The remainder of this paper is organized as follows. Analytically, the propagation measurement, the measurement setup, and the measurement procedure are described in Section 2. The measurement data processing and analysis method are presented in Section 3. Specially, the results of the channel parameters extracted from the measured data and the simulated data are presented in Section 4. Finally, Section 5 is devoted to conclusions summarizing this work.

2. Measurement Campaigns in the High-Speed Railway Station Scenarios

2.1. Measurement Environment. The mmWave massive MIMO channel measurements were conducted based on the time domain channel detector system developed by Keysight in the high-speed railway station scenarios of Qingdaobei, in Qingdao, China. Figure 1(a) is the top view of the measurement environment, and Figure 1(b) shows a map of the position of transmitter (Tx) and the position of receiver (Rx). The whole waiting hall covers an area of $352 \times 213\,m^2$. The height of waiting hall is about 9 m. There are scatterers such as reception desk, seats, charging desk, power distribution room, shop, escalator, toilet, garbage can, flower beds, and billboard in the waiting hall. The reception desk dimensions are approximately $46 \times 4 \times 1.5\,m^3$, which is distributed on the central axis of the waiting hall. There are several rows of waiting chairs on both sides of the service desk, and the size of each row is about $0.8 \times 18.6 \times 0.5\,m^3$. The shop dimensions are approximately $8.5 \times 8.5 \times 3\,m^3$. The wall, ceiling, and floor are made of concrete. The seats are made of stainless steel, and the windows are made of laminated glass. Some metal scatterers presented in the waiting hall make it a rich-multipath scenario.

2.2. Measurement Setup and Procedure. A sliding correlator channel sounder is used to conduct the measurement campaigns at 28 GHz. Figure 2(a) shows the photograph of the Tx and Rx apparatuses. The mmWave MIMO channel sounding system diagram is shown in Figure 2(a). The photographs of measurement setup are shown in Figure 2(b). The height of the Tx antenna is kept fixed at approximately 2.6 m above the ground. At the Tx, a pseudorandom-noise (PN) code with good autocorrelation is generated, and an omnidirectional antenna with 3 dBi gain is used. A power amplifier (PA) with 30 dB gain and low-noise amplifiers (LNA) with 34 dB gain are used to improve the signal-noise-ratio (SNA). On the Rx side, 8-element uniform linear array (ULA-8) with 5 dBi gain is utilized. The height between the center of the ULA-8 and the floor is about 1.85 m. The testbed's noise floor is around −67 dBm. The maximum path loss is roughly up to 102 dB. The correlation operation is applied to the transmitted code and received code. In the sounding system, we use the approach of wideband signal correlation, switching at transmitter and parallel acquisition at receiver. In the calibration connection, the output of the amplifier at the Tx is connected with the input of the LNA at the Rx, and an attenuator is added in the middle. The main components of the channel sounding system and the calibration method are described in [31]. After removing the responses of the measurement system, the channel impulse response can be obtained in the high-speed railway station environment. Moreover, the measurement system is tuned at 28 GHz with 500 MHz bandwidth. The measurable delay resolution is 2 ns. The detailed parameters of channel sounding system are shown in Table 1 and the specifications of the channel sounder have been developed in [32].

During the measurement, the antennas are always boresight-aligned between the Tx antenna and Rx antenna, namely, the normal direction of the antenna array points to the Tx antenna. The separation of the 8-ULA elements is 5.36 mm, which is equal to the $\lambda/2$ at 28 GHz. The array antenna moves 8 times in both horizontal and vertical directions, and the distance of each movement is $\lambda/2$, forming a virtual array with the size of $8 \times 8 \times 8$ as shown in Figure 3. The Tx-1 indicated by red triangle is located between the waiting seats, and Tx-2 indicated by red triangle is fixed next to the hot water supply room as shown in Figure 1(b). A total of 33 Rx positions are measured including 21 LOS points (Tx-1, Rx 1-21) and 12 NLOS points (Tx-2, Rx 22-33). In order to prevent the influence of moving of waiting passengers on the accuracy of measured results, the measurements are conducted early in the morning. Therefore, the environment is time-invariant.

3. Measurement Data Processing and Analysis Method

3.1. SAGE Algorithm. In order to estimate channel propagation parameters from the measurement data, such as DS, complex amplitude, azimuth angle of arrival (AAoA), elevation angle of arrival (EAoA), azimuth angle of departure (AAoD), elevation angle of departure (EAoD), and doppler frequency shift of the MPCs, high-resolution SAGE algorithm is widely used [33, 34]. The received signal vector, assumed to consist of L paths, can be expressed as

$$\mathbf{Y}(t) = \sum_{l=1}^{N} \mathbf{s}(t; \boldsymbol{\Theta}_l) + \sqrt{\frac{N_0}{2}}\mathbf{N}(t), \tag{1}$$

where N_0 is a positive constant, and $\mathbf{N}(t)$ is the complex white Gaussian noise. $\mathbf{s}(t; \Theta_l)$ is the signal contributed by the l thpath at the Rx array, which can be expressed as

$$\mathbf{s}(t; \boldsymbol{\Theta}_l) = \alpha_l \exp\{j2\pi\nu_l t\}\mathbf{c}(\boldsymbol{\Omega}_l)u(t - \tau_l), \tag{2}$$

where $\Theta_l = [\alpha_l, \theta_{r,l}, \varphi_{r,l}, \theta_{t,l}, \varphi_{t,l}, \tau_l, \nu_l,]$, $l = 1, 2, \ldots, L$ represents the vector of the parameters of the l th propagation path. α_l, $\theta_{r,l}$, $\varphi_{r,l}$, $\theta_{t,l}$, $\varphi_{t,l}$, τ_l, and ν_l denote the complex amplitude, EAoA, AAoA, EDoA, ADoA, DS, and doppler frequency shift. $u(t)$ is the transmitted signal. $\mathbf{c}(\Omega) = [c_1(\Omega), \ldots, c_M(\Omega)]^T$ denotes the steering vector of the Rx array consisting of M elements, and the specific components can be expressed as [35]

$$c_m(\boldsymbol{\Omega}) = f_m(\boldsymbol{\Omega})\exp\left(j2\pi\nu_l t\lambda^{-1}\langle e(\boldsymbol{\Omega}), r_m\rangle\right), \quad m = 1, \ldots, M. \tag{3}$$

where $f_m(\Omega)$, λ and $e(\Omega)$ denote the antenna radiation pattern, the wavelength, and the unit vector.

$$e(\boldsymbol{\Omega}) = [\cos(\varphi_l)\sin(\theta_l),\ \sin(\varphi_l)\sin(\theta_l),\ \cos(\theta_l)]^T,$$
$$\langle e(\boldsymbol{\Omega}), r_m\rangle = [x_m - \mathrm{d}x, y_m - \mathrm{d}y, z_m - \mathrm{d}z]e(\boldsymbol{\Omega}). \tag{4}$$

where x_m, y_m and z_m are the position coordinates of the m th antenna element. $\mathrm{d}x = \mathrm{d}y = \mathrm{d}z = 5.36$ mm, which is equal to the $\lambda/2$ at 28 GHz. Because the measurement environment

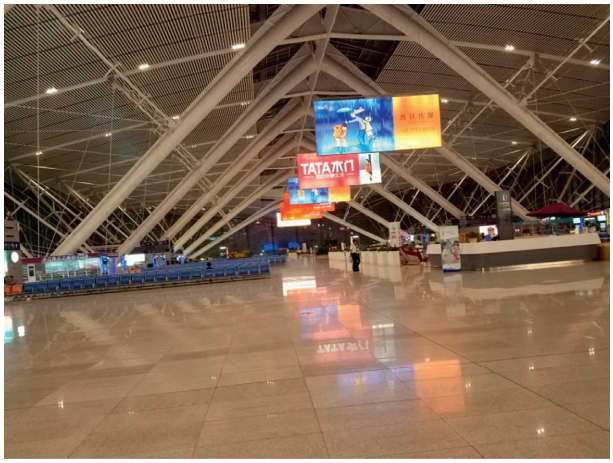

(a)

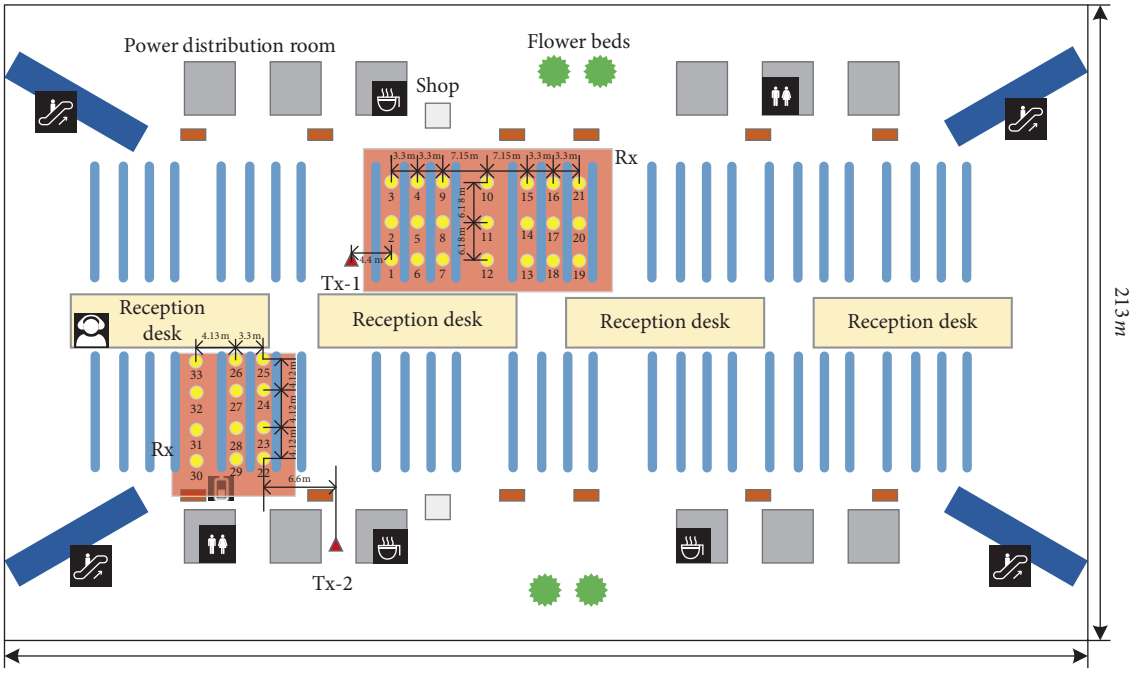

(b)

Figure 1: Measurement environment. (a) Top view of the measurement environment, (b) the position of Tx and the position of Rx.

is quasistatic, the doppler frequency shift is not considered in the algorithm.

The coordinate-wise updating procedure to obtain the estimate $\widehat{\Theta}_l''$ given the previous estimate $\widehat{\Theta}_l'$ is as follows:

$$\widehat{\tau}_l' = \arg\max_{\tau_l}\left\{\left|z\left(\widehat{\Omega}_l', \tau; \widehat{\mathbf{x}}_l\left(t; \widehat{\Theta}_l'\right)\right)\right|\right\},$$

$$\widehat{\Omega}_l'' = \left(\widehat{\varphi}_l'', \widehat{\theta}_l''\right) = \arg\max_{\Omega_l}\left\{\left|z\left(\Omega_l, \widehat{\tau}_l''; \widehat{\mathbf{x}}_l\left(t; \widehat{\Theta}_l'\right)\right)\right|\right\},$$

$$\alpha_l'' = \frac{1}{N^2} z\left(\widehat{\Omega}_l'', \widehat{\tau}_l''; \widehat{\mathbf{x}}_l\left(t; \widehat{\Theta}_l'\right)\right),$$

$$z\left(\Omega, \tau; \widehat{\mathbf{x}}_l\left(t; \widehat{\Theta}_l'\right)\right) = c^H(\Omega)\int u\left(t' - \tau\right)\widehat{\mathbf{x}}_l\left(t'; \widehat{\Theta}_l'\right)\mathrm{d}t',$$

$$\widehat{\mathbf{x}}_l\left(t; \widehat{\Theta}_l'\right) = \begin{cases} \mathbf{y}(t), & l = 1, \\ \mathbf{y}(t) - \sum_{l'=1, l' \neq l}^{L} s\left(t; \widehat{\Theta}_{l'}'\right), & l = 2, \ldots, L, \end{cases} \tag{5}$$

where ^{H} is the conjugate transpose operator.

After many iterations, the estimated parameters will converge to stable values.

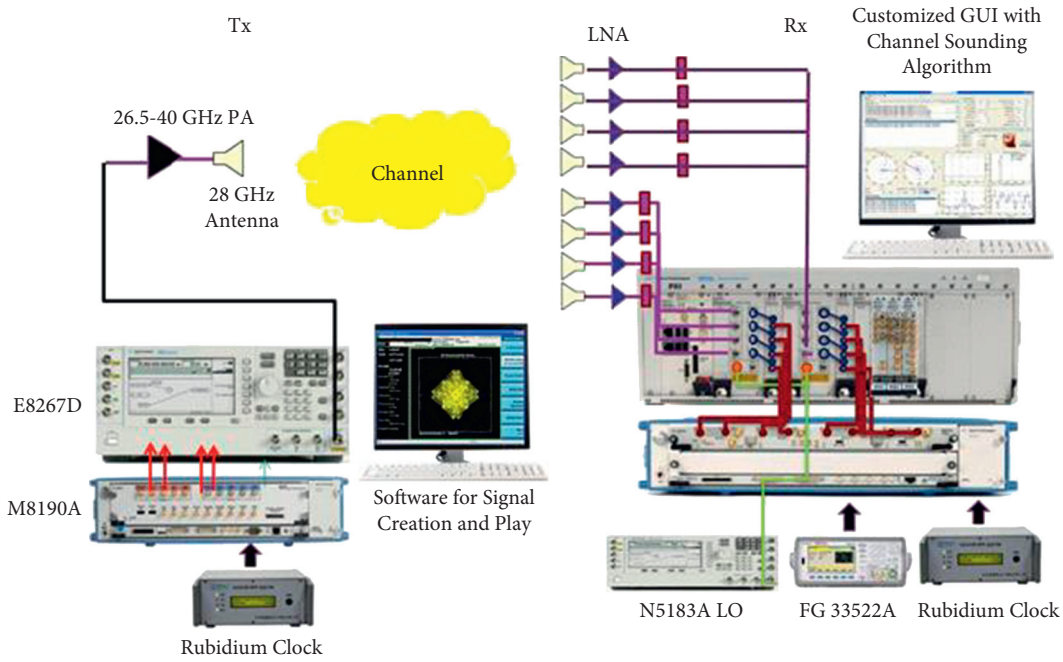

(a)

(b)

Figure 2: Measurement setup. (a) Photograph of the Tx and Rx apparatuses for the channel sounder, (b) measurement setup.

3.2. Ray Tracing Simulations. Extensive channel measurements in typical propagation environment and statistical analysis of a great amount of data can extract the real propagation characteristics of wireless channel. But the measurement is laborious, time-consuming, and expensive, which are great challenges for channel sounding. For this reason, many scientific research teams have proposed deterministic modeling methods, but most deterministic models are electromagnetic methods based on ray tracing simulations. The ray tracing method is used to find the diffracted and reflected rays in a stairwell environment [36]. The channel characteristics and cell coverage are analyzed by developing an efficient 3D ray tracing simulation at 28 GHz [37]. A hybrid model is proposed by combining ray tracing with a propagation graph. By comparing the simulated results with the measured results, it is found that they are consistent, which proves the effectiveness of the method [38, 39]. Then, the hybrid modeling method is applied to predict the reverberant room-to-room radio channel [40]. In addition, a hybrid method is proposed to predict outdoor to indoor coverage based on deterministic 3D outdoor prediction on building surfaces and indoor extension [41]. As

Table 1: Parameters for channel sounding system.

Parameters	Value
Carrier frequency	28 GHz
Bandwidth	500 MHz
Code length	2048 ns
Delay resolution	2 ns
Tx antenna	Omnidirectional
Rx antenna	ULA-8
Tx/Rx antenna height	2.6 m/1.85 m
Rx antenna array size	$8 \times 8 \times 8$
Antenna spacing	$\lambda/2$
Transmission power	−6 dBm
Tx antenna gain	3 dBi
Rx ULA-8 antenna gain	5 dBi
PA power	30 dB
LNA	34 dB

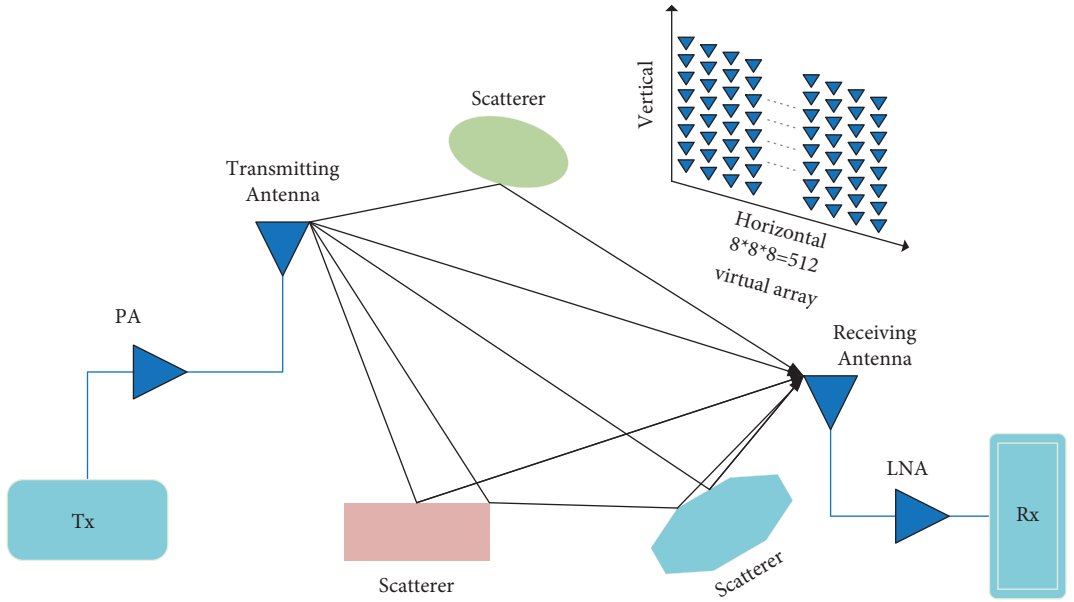

Figure 3: Schematic diagram of virtual array antenna measurement.

another approach of improved ray tracing simulation method, the shooting and bouncing ray tracing/image (SBR/IM) method [42, 43] is an effective method, which is suitable for complex indoor and curved tunnel propagation environment. It can track all the triangular ray tubes bouncing from the transmitter to the receiver with high accuracy and computational efficiency. In this paper, the simulated results are good agreement with measured results over all the measured points. In the simulation, the reflection and diffraction are considered. The maximum number of reflections is set to 4, and the maximum number of diffractions is set to 2. In the simulation, the relative permittivity of wood is 5, and the conductivity is assumed to be 0.01 S/m. In addition, the relative permittivity of concrete is 7, and the conductivity is assumed to be 0.015 S/m based on the material properties at 28 GHz [44, 45].

4. Measurement Results and Simulation Results

4.1. Path Loss Model. PL models are commonly used to illustrate the channel effects caused by the surrounding environment, which estimate the attenuation over distance of propagating signals and are crucial for predicting the coverage probability of wireless communication systems [46, 47]. In our measurement, the link budget to calculate the path loss in dB is [48]

$$\mathrm{PL}[\mathrm{dB}] = P_T + G_T + G_R + G_{\mathrm{RF}} - P_R, \tag{6}$$

where P_T and P_R are the power generated by the signal generator and the received power at 28 GHz, respectively, in dB. G_T and G_R are the gains of the Tx and Rx antennas, respectively, in dB. G_{RF} is the cumulative gain by the radio components.

In this work, two kinds of PL models are investigated based on the measurements and simulations. First, the common PL model, which is the close-in (CI) free-space reference distance PL model [49], provides the advantage of easily comparing PL in terms of different scenarios and different frequency bands. The PL in the CI model is given by

$$\mathrm{PL}^{\mathrm{CI}}(d)[\mathrm{dB}] = \mathrm{FSPL}(f, d_0) + 10n\log_{10}\left(\frac{d}{d_0}\right) + X_\sigma^{\mathrm{CI}}, \quad (7)$$

where $\mathrm{FSPL}(f, d_0) = 20\log_{10}(4\pi f d_0/c)[\mathrm{dB}]$ is the Friis free-space PL in dB. $d_0 = 1$ m is the close-in free-space reference distance. f is the carrier frequency in GHz. c is the speed of light. n denotes the path loss exponent (PLE). d is the distance between transmitter and receiver, and X_σ^{CI} is a zero-mean Gaussian random variable with a standard deviation σ in dB. The optimization minimum mean square error (MMSE) technique is used to calculate PLE by minimizing σ over all the measured channel samples. The physical interpretation of $n = 2$ corresponds to a free-space path loss.

Another PL model is called the floating-intercept (FI) PL model, which is popularly used in several 3GPP standards and WINNER II [50, 51]. The FI model, which is also a single frequency PL model, is defined as

$$\mathrm{PL}^{\mathrm{FI}}(d)[\mathrm{dB}] = \alpha + 10\beta\log_{10}(d) + X_\sigma^{\mathrm{FI}}, \quad (8)$$

where α is a frequency-independent term, which is the floating-intercept in dB, β is a distance dependent term, and X_σ^{FI} is a zero-mean Gaussian random variable with a standard deviation σ in dB derived from MMSE closed-form optimization. Moreover, we compared the measured results and simulated results to verify the accuracy of channel model.

Figure 4 shows CI models and FI models in the high-speed railway station scenarios, and corresponding parameters are presented in Table 2. At the LOS regions, the n is 1.72 and 1.78 for the measurement and simulation, respectively. From the table, we can see that PLEs in LOS scenarios are less than 2. This is probably due to the superposition of multipaths reflected by wall and ground. The values of the PLEs are approximately equal to those of other previous works [16, 18, 52–55]. It is seen that the measured PLE and simulated PLE of CI models are 2.41 and 2.46 for NLOS regions, respectively. The PLEs for NLOS are higher than those for LOS, and the PLEs for NLOS are observed to be higher than 2. An obvious explanation for this is that there have different dominating propagation mechanisms due to different scatterers in the high-speed railway station scenarios. As indicated in Table 2, the standard deviations for CI models vary between 0.74 dB and 2.14 dB for LOS regions, and the standard deviations for CI models vary between 1.04 dB and 1.48 dB for NLOS regions, respectively. In addition, results are slightly different than those in [46] due to different thresholding techniques in postprocessing methods. The standard deviation (sigma in dB) in the NLOS is smaller than the one in LOS for both models. There is a possible explanation that there are few measurement points in NLOS scenarios, and the measurement points are relatively concentrated. The comparison between the measured results and simulated results in the LOS and NLOS regions in the high-speed railway station scenarios shown in Figure 4 proves that the method of ray tracing simulation is valid for evaluating the mmWave massive MIMO channel at 28 GHz.

In Figure 4 we also can see that the CI model has a higher σ compared to the FI models, as the FSPL term of CI model is calculated based on a mathematical model, and the FI model can tune two variables to be better matched with the measured and simulated data. In the LOS regions, the α is 64.14 dB and 64.81 dB for the measurement and simulation, respectively, while, in the NLOS regions, the α is 70.36 dB and 63.37 dB for the measurements and simulation, respectively. It is worth noting that the β of the FI path loss models of measured results is found to be less than 2 at the NLOS regions. This can be attributed to the lack of sensitivity of the FI model in coordinating the physical impact of environmental loss with the distance between the Tx and Rx, indicating the higher accuracy and reliability of CI models than FI models. Moreover, the standard deviations for FI models vary between 0.41 dB and 2.08 dB for LOS regions, and the standard deviations for FI models vary between 1.02 dB and 1.22 dB for NLOS regions, respectively.

4.2. Power Delay Profile. The maximum number of iterations of SAGE algorithm is 45. The quantization precision of the SAGE algorithm is 1 ns and 1°. The number of waves to be estimated is set to $L = 30$. The initialization is demonstrated by means of successive cancellation scheme, which is described in detail in [33]. The antenna array allows an unambiguous elevation estimation in the range of $[0°, 180°)$ and azimuth estimation in the range of $[0°, 360°)$. The received signal strength of 512 virtual antenna elements is measured at 1024 sampling times.

In wireless communication systems, the PDP represents the signal power of the receiver at each time, which can identify the arrival delay of multipath signal to a certain extent [56]. The received signal energy can be calculated from the measured multipath profile. The PDPs obtained from the measured, reconstructed array out signals and residual signals for Rx-8 in LOS scenarios and Rx-27 in NLOS scenarios are indicated as shown in Figures 5 and 6, respectively. There is an obvious multipath signal around 420 ns for Rx-8 in LOS scenarios, and there are three obvious multipath signals around 420 ns, 500 ns, and 680 ns for Rx-27 in NLOS scenarios. Moreover, it is obvious that there is a good match between the measured PDP and reconstructed PDP. The residual PDP is close to 0 dB for Rx-8 and Rx-27, which verifies the correctness and effectiveness of large-scale MIMO channel parameters extraction based on SAGE algorithm in the high-speed railway waiting hall scenarios.

4.3. Time Dispersion Analysis. The root-mean-square delay spread (RMS DS) is an important parameter used to characterize the temporal dispersive properties or frequency selectivity of multipath channels [57]. The mean excess delay τ_m is defined as the first moment of the PDP.

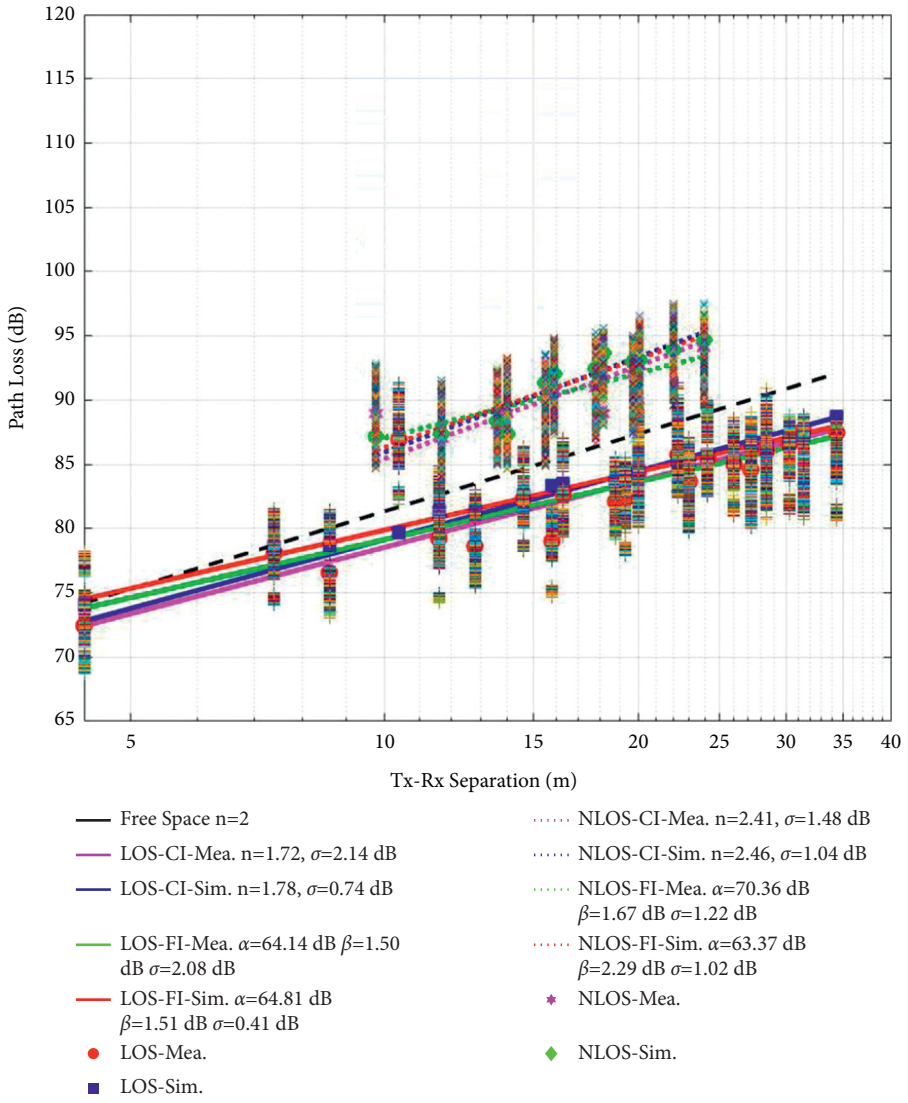

Figure 4: Path loss variation with Tx-Rx separation distance.

Table 2: Parameters for the CI and FI path loss models in the high-speed railway station scenarios in terms of LOS and NLOS scenarios at 28 GHz.

Scenarios	Env.		CI		FI		
			n	σ (dB)	α	β (dB)	σ (dB)
High-speed railway station scenarios	LOS	Mea.	1.72	2.14	64.14	1.50	2.08
		Sim.	1.78	0.74	64.81	1.51	0.41
	NLOS	Mea.	2.41	1.48	70.36	1.67	1.22
		Sim.	2.46	1.04	63.37	2.29	1.02

$$\tau_m = \frac{\sum_k a_k^2 \tau_k}{\sum_k a_k^2} = \frac{\sum_k P(\tau_k)\tau_k}{\sum_k P(\tau_k)}, \tag{9}$$

where a_k, τ_k and $P(\tau_k)$ are the path amplitude, the delay time, and the path gain of the k th MPC, respectively. The RMS DS (τ_{rms}) is defined as the square-root of the second central moment of the normalized PDP

$$\tau_{\text{rms}} = \sqrt{\tau_m^2 - (\tau_m)^2}, \tag{10}$$

where

$$\tau_m^2 = \frac{\sum_k a_k^2 \tau_k^2}{\sum_k a_k^2} = \frac{\sum_k P(\tau_k)\tau_k^2}{\sum_k P(\tau_k)}. \tag{11}$$

The RMS DS is calculated based on the SAGE algorithm. Figure 7 shows the cumulative distribution function (CDF) for the RMS delay spread for LOS Rx-8, LOS Rx-16, NLOS Rx-27, and NLOS Rx-33 at 28 GHz. The Kolmogorov-Smirnov (K-S) hypothesis test is used to determine the goodness-of-fit of

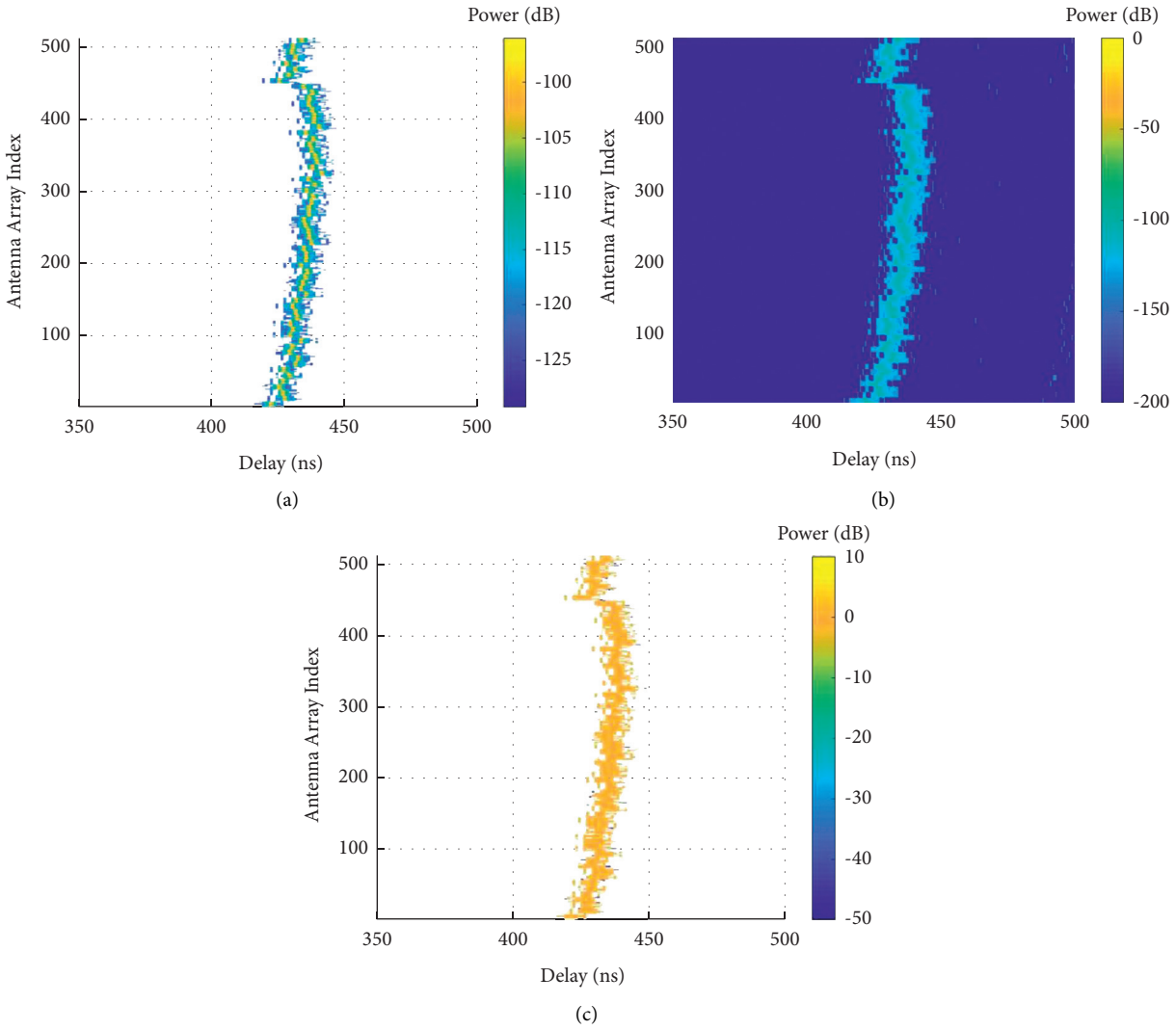

Figure 5: PDP of Rx-8 in LOS scenarios. (a) Measured PDP of Rx-8, (b) reconstructed PDP of Rx8, (c) residual PDP of Rx-8.

distribution at 5% significance. The results lead to an observation that the Gaussian distribution provides good fit to the measured data of RMS delay spread for LOS and NLOS scenarios as shown in Figure 7. The statistics of RMS DS are addressed in Table 3. The minimum RMS DS values are 3.75 ns and 15.65 ns for Rx-8 and Rx-16 in LOS scenario, respectively. The maximum RMS DS values are 10.31 ns and 31.42 ns for Rx-8 and Rx-16 in LOS scenario, respectively. The minimum RMS DS values are 21.40 ns and 22.74 ns for Rx-27 and Rx-33 in NLOS scenario, respectively. Moreover, the maximum RMS DS values are 39.98 ns and 61.83 ns for Rx-27 and Rx-33 in NLOS scenario, respectively. A total of 90% of the RMS DS is found to be less than 6 ns and 30 ns for Rx-8 and Rx-16 in LOS scenario, respectively. A total of 90% of the RMS DS is found to be less than 36 ns and 54 ns for Rx-27 and Rx-33 in NLOS scenario, respectively. For the NLOS scenario, there is no directed path. It is seen that the RMS DS values in NLOS locations are generally found to have higher values than LOS locations due to the obstructions of scattering objects in NLOS locations, which has consistent effects in [58].

4.4. Angular Dispersion Properties. Similar to the RMS DS, the angular spread is also a significant parameter in mmWave massive MIMO channel [59]. It shows the extent of the space selectivity, so it is related to the spatial correlation in multiple antennas systems. The root-mean-square angular spread of azimuth (RMS ASA) is defined as the second-order moment of the power spectrum and is given by [59]

$$\sigma_{\phi}^{Rx} = \sqrt{\frac{\sum_i \left|\exp\left(j\phi_i^{Rx}\right) - \mu_{\phi}^{Rx}\right|^2 \alpha_i^2}{\sum_i \alpha_i^2}}, \tag{12}$$

where μ_{ϕ}^{Rx} is the mean angle of arrival and is defined as

$$\mu_{\phi}^{Rx} = \frac{\sum_i \exp\left(j\phi_i^{Rx}\right)\alpha_i^2}{\sum_i \alpha_i^2}. \tag{13}$$

By replacing ϕ^{Rx} with θ^{Rx}, the angular spread of elevation (EAS) σ_{θ}^{Rx} can be estimated.

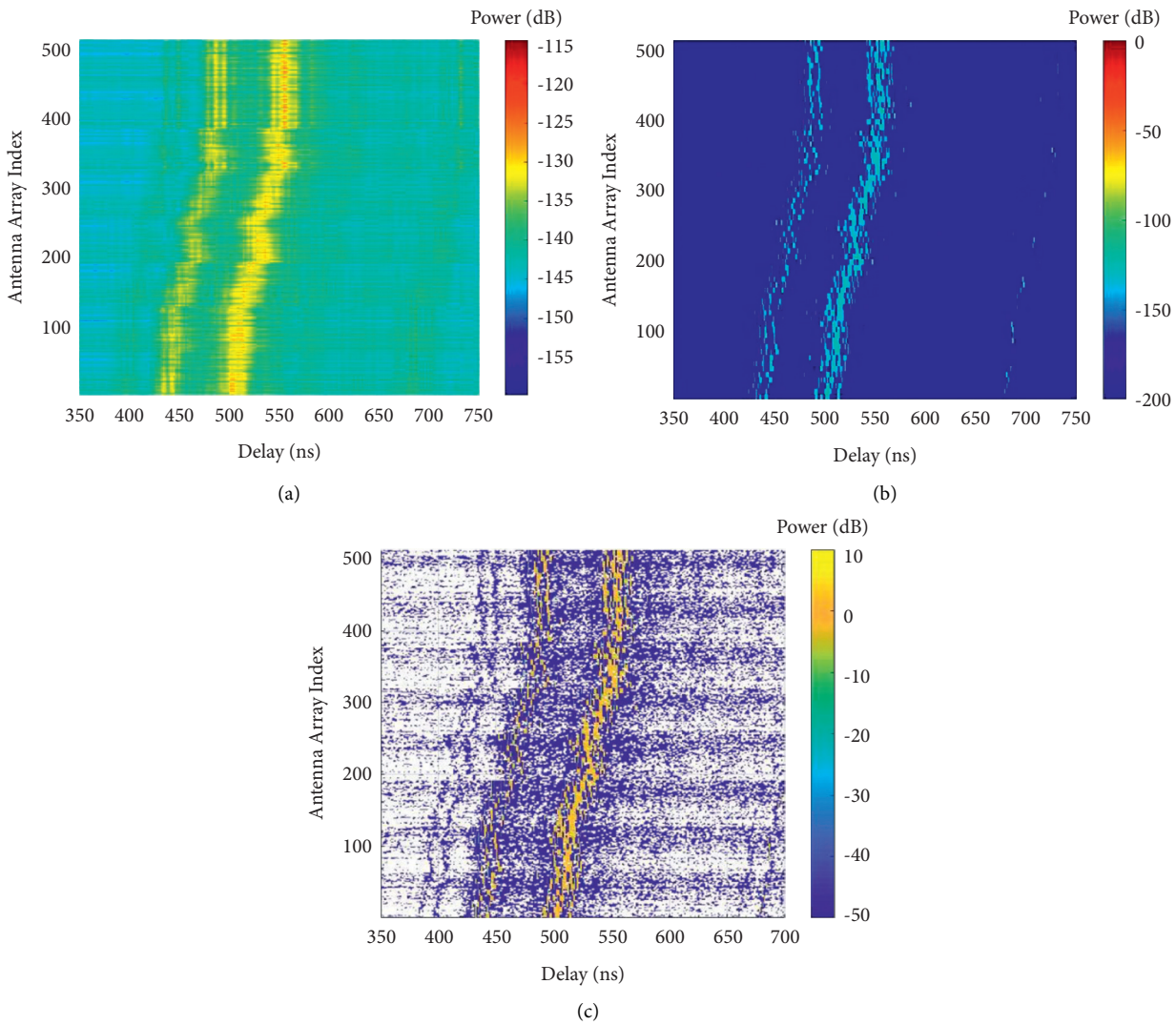

Figure 6: PDP of Rx-27 in NLOS scenarios. (a) Measured PDP of Rx-27, (b) reconstruction PDP of Rx-27, (c) residual PDP of Rx-27.

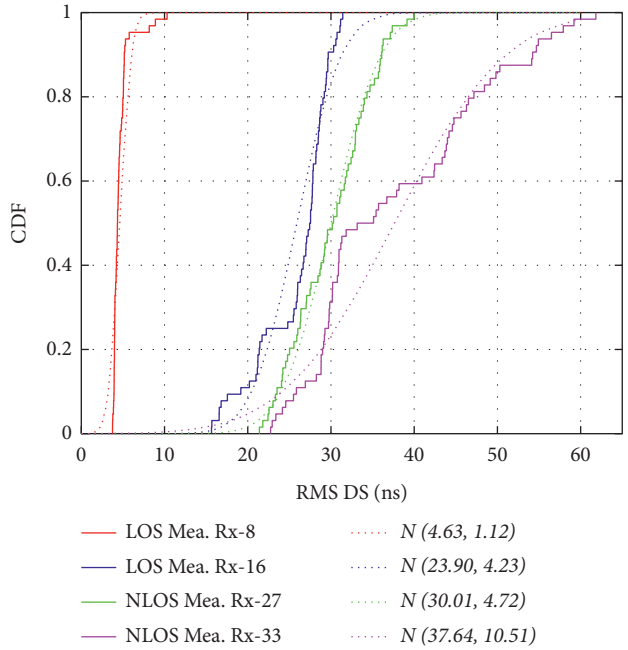

Figure 7: RMS delay spread in LOS and NLOS scenarios.

Table 3: RMS delay spread values for LOS and NLOS scenarios.

Scenarios			Fitted parameters				
			μ (ns)	σ (ns)	Max (ns)	Min (ns)	Median (ns)
High-speed railway station scenarios	Rx-8	LOS	4.63	1.12	10.31	3.75	4.34
	Rx-16	LOS	23.90	4.23	31.42	15.65	27.49
	Rx-27	NLOS	30.01	4.72	39.98	21.40	30.23
	Rx-33	NLOS	37.64	10.51	61.83	22.74	34.13

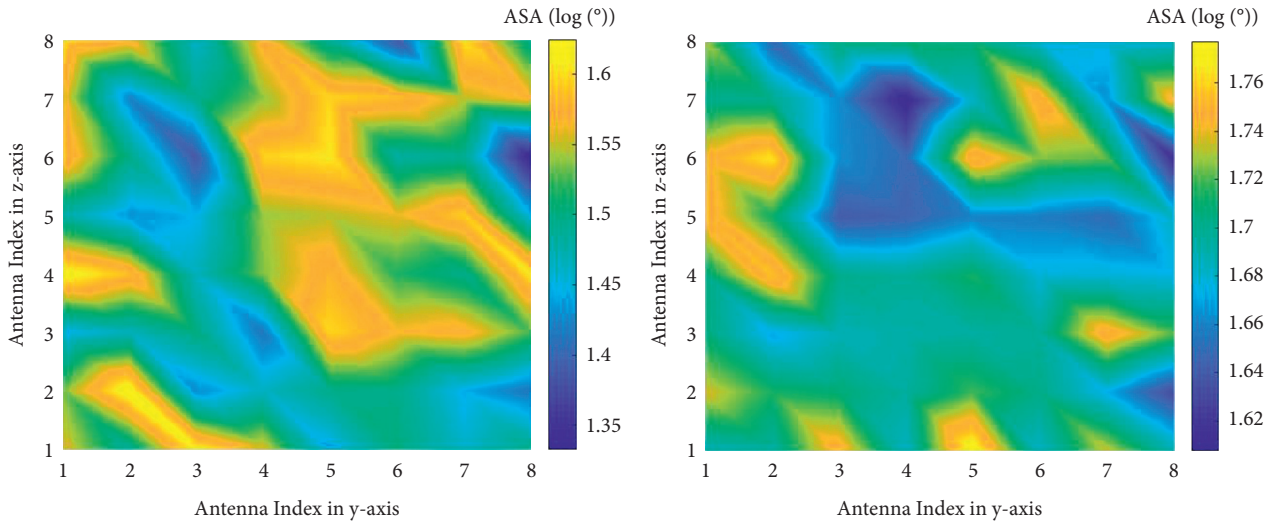

Figure 8: RMS ASA. (a) RMS ASA of Rx-8. (b) RMS ASA of Rx-27.

The RMS ASA and RMS ESA values can be calculated using the equations of (12) and (13), respectively. The values of RMS ASA and RMS ESA calculated by SAGE algorithm for Rx-8 in LOS scenarios and Rx-27 in NLOS scenarios are shown in Figures 8 and 9, respectively. It can be seen that the RMS angular spread value of NLOS scenarios is higher than that of LOS scenarios. This is probably due to the less reflectors and scatterers in LOS scenarios and obstructions between Tx and Rx for NLOS scenarios. Moreover, the range of ESA is smaller than the range of ASA. This shows that the MPCs spread in the horizontal direction are more significant than those in the vertical direction in the high-speed railway waiting hall environment. These results are consistent with the previous studies in [15, 26, 59].

4.5. Clustering of MPCs. The K-mean algorithm is a typical algorithm that can be used to divide multipath signals into multiple clusters. A cluster is defined as a group of MPCs with similar AoA and DS. Multipath components distance (MCD) is a common measure standard to distinguish clusters. The MCD between the ith and jth MPCs is calculated as [22]

$$\mathrm{MCD}_{ij} = \sqrt{\left(\mathrm{MCD}_{\tau}^{ij}\right)^2 + \left(\mathrm{MCD}_{\mathrm{AoA}}^{ij}\right)^2}, \tag{14}$$

where MCD_{τ}^{ij} and $\mathrm{MCD}_{\mathrm{AoA}}^{ij}$ are the MCD in time-delay domain and angle domain, respectively.

$$\begin{aligned} \mathrm{MCD}_{\tau}^{ij} &= \xi \frac{\left|\tau_j - \tau_i\right|\sigma_{\tau}}{\Delta\tau_{\max}^2}, \\ \mathrm{MCD}_{\mathrm{AoA}}^{ij} &= \left\|\boldsymbol{\Omega}_j - \boldsymbol{\Omega}_i\right\|, \\ \Delta\tau_{\max} &= \max\left\{\left|\tau_i - \tau_j\right|; \quad \forall i, j \in [1, \ldots, L]\right\}, \end{aligned} \tag{15}$$

where $\Omega_k = [\cos(\varphi_k)\sin(\theta_k),\ \sin(\varphi_k)\sin(\theta_k),\ \cos(\theta_k)]^T$. $\tau$is the RMS DS, and $\Delta\tau_{\max}$ is the delay difference between the MPCs, maximized over all of MPCs. ξ is the delay weighting factor, which balances the relative importance weights of AoA MCD and DS MCD. For the measured data, $\xi = 8$ and a predefined threshold $\mathrm{MCD}_{\mathrm{th}} = 0.5$ are suitable.

For the sake of space and clarity, only two examples of multipath clustering results are considered at the location of the Rx-8 for LOS scenarios and at the location of the Rx-27 for NLOS scenarios, respectively, as shown in Figure 10. A common cluster is represented by a distinctive color. It shows that the number of clusters is six for Rx-8 and nine for Rx-27, respectively. For Rx-8, the clustering effect is obvious, and the EAoA of red cluster is about 90°, which corresponds to the LOS cluster. For Rx-27, according to delays of MPCs, there is no direct path, and the MPCs of the channel in multipath arriving in various directions are abundant, which indicates multiple reflections or scattering due to scatterers and building construction materials in the waiting hall of

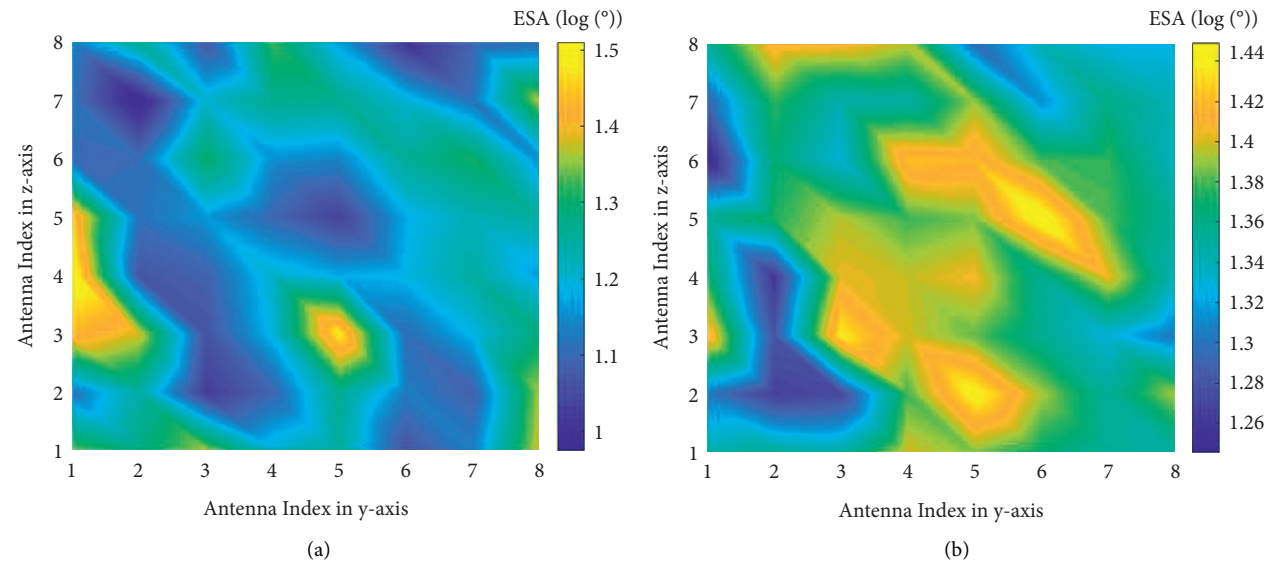

Figure 9: RMS ESA. (a) RMS ESA of Rx-8. (b) RMS ESA of Rx-27.

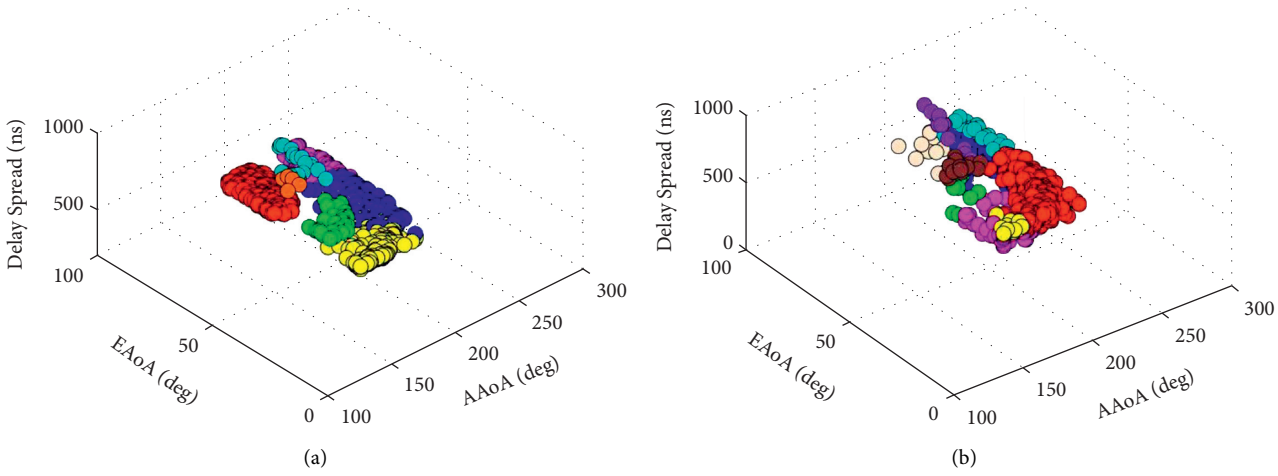

Figure 10: Clustered MPCs. (a) Rx-8 in LOS scenarios. (b) Rx-27 in NLOS scenarios.

high-speed railway. As comparison, the value of the numbers of clusters for Rx-8 is significantly less than that of the results in the published literature [60, 61]. The reason is that the number of clusters rely on the measurement environment, the measurement dynamic range, the algorithm of clustering, the denoising threshold, and so on.

5. Conclusion

This paper presents mmWave massive MIMO channel measurements in the high-speed railway waiting hall environments at 28 GHz. The multipath components parameters are extracted and estimated from the measurement data. Then, propagation characteristics are simulated based on the improved ray tracing method. The correctness and effectiveness of the improved ray tracing method are verified. Moreover, large-scale path loss and temporal statistics are provided. The CI and FI path loss model parameters are estimated. The Gaussian distribution provides good fit to the measured data of RMS delay spread for LOS and NLOS scenarios. Finally, multipath clustering is identified using the multipath component distance. The above-mentioned results can improve the shortcomings of wireless channel propagation characteristics at the special frequency bands. It provides theoretical basis for the optimization of 5G and B5G wireless communication system.

In addition, when there are human body or vehicle moving in the wireless channel, the propagation characteristics will change greatly at mmWave band or terahertz band. At present, ray tracing simulation is used to model the fast changing channel, but there is still a lack of actual measurement. In the future, more automatic measurement equipment should be added to improve the accuracy of the actual measurement. Meanwhile, methods such as neural network or machine learning can be introduced to model the data, so as to achieve the purpose of high-precision channel

modeling. Moreover, the advantages of mmWave Massive MIMO configuration and the performance of mmWave Massive MIMO virtual arrays need further study.

Data Availability

The data used to support the findings of this study are available from the corresponding author upon request.

Conflicts of Interest

The authors declare that there are no conflicts of interest regarding the publication of this paper.

Acknowledgments

This work was supported in part by the National Natural Science Foundation of China (61871232) and in part by the Postgraduate Research & Practice Innovation Program of Jiangsu Province (KYLX16_0650). Moreover, the authors are incredibly thankful to Prof. Leke Lin from China Research Institute of Radiowave Propagation, Qingdao, for providing them an opportunity to carry out the radio propagation measurement.

References

[1] J. Bian, C.-X. Wang, X. Gao, X. You, and M. Zhang, "A general 3D Non-stationary wireless channel model for 5G and beyond," *IEEE Transactions on Wireless Communications*, vol. 20, no. 5, pp. 3211–3224, 2021.

[2] K. Hassan, M. Masarra, M. Zwingelstein, and I. Dayoub, "Channel estimation techniques for millimeter-wave communication systems: achievements and challenges," *IEEE Open Journal of the Communications Society*, vol. 1, pp. 1336–1363, 2020.

[3] T. S. Rappaport, G. R. MacCartney Jr., M. K. Samimi, and S. Sun, "Wideband millimeter-wave propagation measurements and channel models for future wireless communication system design," *IEEE Transactions on Communications*, vol. 63, no. 9, pp. 3029–3056, 2015.

[4] W. Roh, J.-Y. Seol, J. Park et al., "Millimeter-wave beamforming as an enabling technology for 5G cellular communications: theoretical feasibility and prototype results," *IEEE Communications Magazine*, vol. 52, no. 2, pp. 106–113, 2014.

[5] S. Hur, T. Kim, D. J. Love, J. V. Krogmeier, T. A. Thomas, and A. Ghosh, "Millimeter wave beamforming for wireless backhaul and access in small cell networks," *IEEE Transactions on Communications*, vol. 61, no. 10, pp. 4391–4403, 2013.

[6] M. Shafi, A. F. Molisch, P. J. Smith et al., "5G: a tutorial overview of standards, trials, challenges, deployment, and practice," *IEEE Journal on Selected Areas in Communications*, vol. 35, no. 6, pp. 1201–1221, 2017.

[7] J.-H. Zhang, P. Tang, L. Yu, T. Jiang, and L. Tian, "Channel measurements and models for 6G: current status and future outlook," *Frontiers of Information Technology & Electronic Engineering*, vol. 21, no. 1, pp. 39–61, 2020.

[8] J.-Y. Lee, J.-H. Lee, and S.-C. Kim, "Improving the accuracy of millimeter-wave ray-tracing simulations by modeling roadside trees," *IEEE Antennas and Wireless Propagation Letters*, vol. 18, no. 1, pp. 162–166, 2019.

[9] T. S. Rappaport, R. W. Heath Jr., R. C. Daniels, and J. N. Murdock, *Millimeter Wave Wireless Communications*, Person/Prentice Hall, Hoboken, NJ, USA, 2015.

[10] F. Rusek, D. Persson, B. K. Larsson, T. L. Marzetta, and F. Tufvesson, "Scaling up MIMO: opportunities and challenges with very large arrays," *IEEE Signal Processing Magazine*, vol. 30, no. 1, pp. 40–60, 2013.

[11] X. Gao, L. Dai, S. Han, Chih-Lin I, and R. W. Heath, "Energy-efficient hybrid analog and digital precoding for mmWave MIMO systems with large antenna arrays," *IEEE Journal On Selected Areas in Communications*, vol. 34, no. 4, pp. 998–1009, 2016.

[12] C.-X. Wang, J. Huang, H. Wang, X. Gao, X. You, and Y. Hao, "6G wireless channel measurements and models: trends and challenges," *IEEE Vehicular Technology Magazine*, vol. 15, no. 4, pp. 22–32, 2020.

[13] J. Huang, C.-X. Wang, H. Chang, J. Sun, and X. Gao, "Multi-frequency multi-scenario millimeter wave MIMO channel measurements and modeling for B5G wireless communication systems," *IEEE Journal On Selected Areas in Communications*, vol. 38, no. 9, pp. 2010–2025, 2020.

[14] B. Ai, K. Guan, R. He et al., "On indoor millimeter wave massive MIMO channels: measurement and simulation," *IEEE Journal on Selected Areas in Communications*, vol. 35, no. 7, pp. 1678–1690, 2017.

[15] P. Zhang, B. Yang, C. Yi, H. Wang, and X. You, "Measurement-based 5G millimeter-wave propagation characterization in vegetated suburban macrocell environments," *IEEE Transactions on Antennas and Propagation*, vol. 68, no. 7, pp. 5556–5567, 2020.

[16] J. Ko, Y.-J. Cho, S. Hur et al., "Millimeter-wave channel measurements and analysis for statistical spatial channel model in in-building and urban environments at 28 GHz," *IEEE Transactions On Wireless Communications*, vol. 16, no. 9, pp. 5853–5868, 2017.

[17] N. Iqbal, J. Luo, R. Müller et al., "Multipath cluster fading statistics and modeling in millimeter-wave radio channels," *IEEE Transactions on Antennas and Propagation*, vol. 67, no. 4, pp. 2622–2632, 2019.

[18] A. M. Al-Samman, T. A. Rahman, M. H. Azmi, M. N. Hindia, I. Khan, and E. Hanafi, "Statistical modelling and characterization of experimental mm-Wave indoor channels for future 5G wireless communication networks," *PLoS One*, vol. 11, pp. 1–29, 2016.

[19] K. Haneda, J. Järveläinen, A. Karttunen, M. Kyro, and J. Putkonen, "A statistical spatio-temporal radio channel model for large indoor environments at 60 and 70 GHz," *IEEE Transactions on Antennas and Propagation*, vol. 63, no. 6, pp. 2694–2704, 2015.

[20] S. Salous and S. El-Faitori, "Path loss models and delay spread parameters for the millimeter wave channel in indoor environments," in *Proceedings of the IEEE 14th European Conference on Antennas and Propagation (EuCAP)*, pp. 1–3, Copenhagen, Denmark, March 2020.

[21] M. Ghaddar, I. Ben Mabrouk, M. Nedil, K. Hettak, and L. Talbi, "Deterministic modeling of 5G millimeter-wave communication in an underground mine tunnel," *IEEE Access*, vol. 7, pp. 116519–116528, 2019.

[22] X. Yin, C. Ling, and M.-D. Kim, "Experimental multipath-cluster characteristics of 28-GHz propagation channel," *IEEE Access*, vol. 3, pp. 3138–3150, 2015.

[23] J. Chen, X. Yin, X. Cai, and S. Wang, "Measurement-based massive MIMO channel modeling for outdoor LoS and NLoS environments," *IEEE Access*, vol. 5, pp. 2126–2140, 2017.

[24] S. Li, X. W. Zhao, R. Zhang, and B. Li, "Millimeter-wave channel measurements, modeling and simulation for outdoor microcells at 39 GHz," *Chinese Journal of Radio Science*, vol. 32, pp. 498–506, 2017.

[25] J. -H. Zhang, Z. Zheng, Y. Zhang, J. Xi, X. Zhao, and G. Gui, "3D MIMO for 5G NR: several observations from 32 to massive 256 antennas based on channel measurement," *IEEE Communications Magazine*, vol. 56, no. 3, pp. 62–70, 2018.

[26] A. Bamba, F. Mani, and R. D'Errico, "Millimeter-wave indoor channel characteristics in V and E bands," *IEEE Transactions on Antennas and Propagation*, vol. 66, no. 10, pp. 5409–5424, 2018.

[27] S. Sangodoyin, V. Kristem, A. F. Molisch, R. He, F. Tufvesson, and H. M. Behairy, "Statistical modeling of ultrawideband MIMO propagation channel in a warehouse environment," *IEEE Transactions on Antennas and Propagation*, vol. 64, no. 9, pp. 4049–4063, 2016.

[28] Q. Y. Guo, Y. Wang, X. Liao, C. Jin, J. Zhang, and J. Zhang, "Measurement of millimeter-wave 3D MIMO channel in large indoor environment," in *Proceedings of the IEEE 15th European Conference on Antennas and Propagation (EuCAP)*, pp. 1–5, Dusseldorf, Germany, March 2021.

[29] Z. Hu, W. Ji, H. Zhao, X. Zhai, A. Saleem, and G. Zheng, "channel measurement for multiple frequency bands in subway tunnel scenario," *International Journal of Antennas and Propagation*, vol. 2021, Article ID 9991758, 13 pages, 2021.

[30] X. Zhao, Z. Wang, S. Geng, Y. Zhang, F. Du, and Z. Fu, "Channel sounding, modelling, and characterisation in a large waiting hall of a high-speed railway station at 28 GHz," *IET Microwaves, Antennas & Propagation*, vol. 13, no. 15, pp. 2619–2624, 2019.

[31] W. Zhu and H. W. Kong, "mmWave MIMO channel sounding for 5G," in *Proceedings of the IEEE International Conference on 5G for Ubiquitous Connectivity (5GU)*, pp. 192–197, Akaslompolo, Finland, November 2014.

[32] Y. S. Liu, C. Z. Hou, L. K. Lin et al., "Measurement and comparative analysis of channel parameters of different antenna forms in 5G millimeter wave frequency band," *Chinese Journal of Radio Science*, vol. 36, pp. 422–429, 2021.

[33] B. H. Fleury, M. Tschudin, R. Heddergott, D. Dahlhaus, and K. Ingeman Pedersen, "Channel parameter estimation in mobile radio environments using the SAGE algorithm," *IEEE Journal on Selected Areas in Communications*, vol. 17, no. 3, pp. 434–450, 1999.

[34] B. H. Fleury, X. F. Yin, K. G. Rohbrandt, P. Jourdan, and A. Stucki, "Performance of a high-resolution scheme for joint estimation of delay and bidirection dispersion in the radio channel," in *Proceedings of the IEEE Vehicular Technology Conference (VTC)*, pp. 522–526, Birmingham, USA, August 2002.

[35] X. Wu, C.-X. Wang, J. Sun et al., "60-GHz millimeter-wave channel measurements and modeling for indoor office environments," *IEEE Transactions on Antennas and Propagation*, vol. 65, no. 4, pp. 1912–1924, 2017.

[36] V. A. Fono, L. Talbi, O. A. Safia, M. Nedil, and K. Hettak, "Deterministic modeling of indoor stairwells propagation channel," *IEEE Antennas and Wireless Propagation Letters*, vol. 19, no. 2, pp. 327–331, 2020.

[37] J.-H. Lee, J.-S. Choi, and S.-C. Kim, "Cell coverage analysis of 28 GHz millimeter wave in urban microcell environment using 3-D ray tracing," *IEEE Transactions on Antennas and Propagation*, vol. 66, no. 3, pp. 1479–1487, 2018.

[38] T. Pedersen, G. Steinböck, and B. H. Fleury, "Modeling of reverberant radio channels using propagation graphs," *IEEE Transactions on Antennas and Propagation*, vol. 60, no. 12, pp. 5978–5988, 2012.

[39] G. Steinböck, M. Gan, P. Meissner et al., "Hybrid model for reverberant indoor radio channels using rays and graphs," *IEEE Transactions on Antennas and Propagation*, vol. 64, no. 9, pp. 4036–4048, 2016.

[40] Y. Miao, T. Pedersen, M. Gan, E. Vinogradov, and C. Oestges, "Reverberant room-to-room radio channel prediction by using rays and graphs," *IEEE Transactions on Antennas and Propagation*, vol. 67, no. 1, pp. 484–494, 2019.

[41] V. Degli-Esposti, J. S. Lu, J. N. Wu et al., "A semi-deterministic model for outdoor-to-indoor prediction in urban areas," *IEEE Antennas and Wireless Propagation Letters*, vol. 16, pp. 2412–2415, 2017.

[42] S. D. Li, Y. J. Liu, L. K. Lin et al., "Millimeter wave channel characteristics of outdoor microcellular based on improved ray tracing method and BP neural network algorithm," *Chinese Journal of Radio Science*, vol. 36, pp. 430–442, 2021.

[43] S. D. Li, Y. J. Liu, L. Yao, and W. Cao, "Improved channel model and analysis of the effect of bodies in curved tunnel using ray tracing," *IEEE Antennas and Wireless Propagation Letters*, vol. 19, no. 7, pp. 1162–1166, 2020.

[44] International Telecommunication Union Radiocommunication Sector (ITU-R), "Effects of building materials and structures on radiowave propagation above 100 MHz," Report ITU-R P.2040, International Telecommunication Union, Geneva, Switzerland, 2013.

[45] L. M. Correia and P. O. Frances, "Estimation of materials characteristics from power measurements at 60 GHz," in *Proceedings of the IEEE International Symposium on Personal, Indoor and Mobile Radio Communications, Wireless Networks-Catching the Mobile Future*, vol. 2, pp. 510–513, The Hague, Netherlands, September 1994.

[46] G. R. Maccartney, T. S. Rappaport, S. Sun, and S. Deng, "Indoor office wideband millimeter-wave propagation measurements and channel models at 28 and 73 GHz for ultra-dense 5G wireless networks," *IEEE Access*, vol. 3, pp. 2388–2424, 2015.

[47] S.-d. Li, Y.-j. Liu, L.-k. Lin et al., "Channel measurements and modeling at 6 GHz in the tunnel environments for 5G wireless systems," *International Journal of Antennas and Propagation*, vol. 201715 pages, Article ID 1513038, 2017.

[48] T. S. Rappaport, S. Sun, R. Mayzus et al., "Millimeter wave mobile communications for 5G cellular: it will work!" *IEEE Access*, vol. 1, pp. 335–349, 2013.

[49] S. Sun, T. S. Rappaport, T. A. Thomas et al., "Investigation of prediction accuracy, sensitivity, and parameter stability of large-scale propagation path loss models for 5G wireless communications," *IEEE Transactions on Vehicular Technology*, vol. 65, no. 5, pp. 2843–2860, 2016.

[50] S. Hur, S. Baek, B. Kim et al., "Proposal on millimeter-wave channel modeling for 5G cellular system," *IEEE Journal of Selected Topics in Signal Processing*, vol. 10, no. 3, pp. 454–469, 2016.

[51] P. Kyösti, J. Meinilä, L. Hentilä, and X. Zhao, "WINNER II channel models," IST-4-027756 WINNER II, Technical Report D1.2, European Commission, Brussels, Belgium, 2007.

[52] M. Y. Lei, J. H. Zhang, L. Tian, and D. Du, "28-GHz indoor channel measurements and analysis of propagation characteristics," in *Proceedings of the IEEE 25th International Symposium on Personal, Indoor, and EMC Mobile Radio Communication (PIMRC)*, pp. 208–212, Washington, DC, USA, September 2014.

[53] J. Lee, J. Liang, J. J. Park, and M. D. Kim, "Directional path loss characteristics of large indoor environments with 28 GHz measurements," in *Proceedings of the IEEE 26th International Symposium on Personal, Indoor, and Mobile Radio Communication (PIMRC)*, pp. 2204–2208, Hongkong, China, September 2015.

[54] S. Sun, G. R. MacCartney, and T. S. Rappaport, "Millimeter-wave distance-dependent large-scale propagation measurements and path loss models for outdoor and indoor 5G systems," in *Proceedings of the IEEE 10th European Conference on Antennas and Propagation (EuCAP)*, pp. 1–5, Davos, Switzerland, April 2016.

[55] J. Lee, J. Liang, M.-D. Kim, J.-J. Park, B. Park, and H. K. Chung, "Measurement-based propagation channel characteristics for millimeter-wave 5G Giga communication systems," *ETRI Journal*, vol. 38, no. 6, pp. 1031–1041, 2016.

[56] A. Meijerink and A. F. Molisch, "On the physical interpretation of the saleh-valenzuela model and the definition of its power delay profiles," *IEEE Transactions on Antennas and Propagation*, vol. 62, no. 9, pp. 4780–4793, 2014.

[57] A. F. Molisch, "Statistical properties of the RMS delay-spread of mobile radio channels with independent Rayleigh-fading paths," *IEEE Transactions on Vehicular Technology*, vol. 45, no. 1, pp. 201–204, 1996.

[58] H. Hashemi and D. Tholl, "Statistical modeling and simulation of the RMS delay spread of indoor radio propagation channels," *IEEE Transactions on Vehicular Technology*, vol. 43, no. 1, pp. 110–120, 1994.

[59] B. H. Fleury, "First- and second-order characterization of direction dispersion and space selectivity in the radio channel," *IEEE Transactions on Information Theory*, vol. 46, no. 6, pp. 2027–2044, 2000.

[60] https://www.3gpp.org/DynaReport/38900.htm 3rd Generation Partnership Project, "Study on channel model for frequency spectrum above 6 GHz,".

[61] X. Zhao, S. Li, Q. Wang, M. Wang, S. Sun, and W. Hong, "Channel measurements, modeling, simulation and validation at 32 GHz in outdoor microcells for 5G radio systems," *IEEE Access*, vol. 5, pp. 1062–1072, 2017.